Intensity Correlations and Dynamical Processes in Cavity Quantum Electrodynamics

A Dissertation Presented

by

Stephen Lawrence Mielke

to

The Graduate School

in Partial Fulfillment of the Requirements

for the Degree of

Doctor of Philosophy

in

Physics and Astronomy

State University of New York
at
Stony Brook

May 1998

Chapter 3

Time Response to a Step Excitation

3.1 Introduction

The nonlinearity of the atoms-cavity system yields a rich spectroscopic structure. At intermediate intensities, however, the transmission of the cavity as a function of frequency is multi-valued, which complicates the extraction of information about the frequencies present in the system. A different approach is to look at the time response to step excitation to measure the frequencies present in the resulting oscillations as the system returns to steady state. For a linear system, the Fourier transform of a time response to step excitation measurement is its spectrum. In the nonlinear case, as is the case of our system, the Fourier transform gives a spectrum, different from the transmission spectroscopy result. The Fourier transform of the time response to an infinitesimally small step gives the local eigenvalues of the system, even in a nonlinear regime.

The time response of an atoms-cavity system has been used by several

groups to study the dynamical evolution of the system. Kaluzny *et al.* [6], in the group of Haroche, measured oscillations in Rydberg atoms travelling through a microwave cavity. They prepared the atoms in an excited state and measured the survival probability of atoms in the excited state as a function of atom-cavity interaction time. They found that while in the cavity the atoms oscillated between the excited and less excited state at the rate $g\sqrt{\bar{N}}$, where $\bar{N}$ is the effective number of atoms in the cavity (see Eq. 1.6).

In the optical regime, the time response to a turn-off step excitation of an atoms-cavity system has been studied by Brecha *et al.* [7] in the low intensity limit. They measured the oscillatory response of light transmitted through an atoms-cavity system after the external cavity excitation was suddenly changed from a steady state intensity to a slightly lower intensity (high:low = 6:5). These experiments were able to establish an oscillation frequency dependence on the number of atoms present in the system, in rough agreement with the prediction of Agarwal, $\Omega_0 = g\sqrt{N}$ [2]. Measurements with a larger high:low ratio were not able to resolve oscillations as the system returned to its steady state.

In a condensed matter system, Wang *et al.* [8] measured the coherent exchange of energy between coupled cavity-exciton modes in the nonlinear regime. In this condensed matter system these dynamics take place on the femtosecond time scale.

We performed a set of experiments in which we excited the system with a pulse of light instead of a constant amplitude driving field. We kept the atoms, cavity, and laser on resonance, and measured the intensity of light

transmitted through the cavity as a function of time after the step changes. The parameters g, κ, and $\gamma_\perp$ of our system are all of the order of 3 MHz. In order to probe its dynamical behavior, the step change must be significantly faster, on the order of 100 MHz.

The system starts with the atoms in the ground state with no driving field. After the light is turned on, the field inside the cavity oscillates as it comes to equilibrium at a non-zero steady state. After the oscillations have well disappeared into the noise (15 times the decay time), we turn off the input light and let the system come to a new undriven equilibrium state. The time response to the turn-on probes the dynamics of the system for a non-zero driving field, while the response to the turn-off yields information about the undriven system. Since the system is on resonance, the steady state intensity in the cavity is much lower than it was for the measurements in Chapter 2, where we were on the vacuum Rabi sidebands. We are operating along the central dashed line of Fig. 2.3, or along the lower line of Fig. 2.2, the so-called lower branch of on-resonance optical bistability. We keep the input intensity low enough that the system is always on the lower branch. The output intensity, however, can be momentarily much higher than the steady state for the corresponding input intensity discussed in Chapter 2.

3.2   Model

The temporal evolution of the system is governed by the Maxwell Bloch equations. For a single mode plane travelling wave system on

resonance [25, 29],

$$\frac{dx}{dt} = -\kappa(x - y - 2CP),$$ (3.1)

$$\frac{dP}{dt} = \gamma_\perp(xD - P),$$ (3.2)

$$\frac{dD}{dt} = -\gamma_\parallel[\frac{1}{2}(xP^* + x^*P) + D + 1],$$ (3.3)

with x^* and P^* following the complex conjugate equations of Eq. 3.1 and Eq. 3.2, respectively. $x \equiv \langle \hat{a} \rangle / \sqrt{n_0}$ is the intracavity field and $y \equiv \mathcal{E}/\kappa\sqrt{n_0}$ is the driving term, where $\mathcal{E}$ is the input field amplitude (in units of $1/s$). P is the normalized atomic polarization, and D is the normalized population difference between the upper and lower atomic states, with $D = -1$ representing all atoms in the ground state. $C = C_1 N$ is the many-atom cooperativity. By setting the time derivatives to zero we can find a steady state equation for the system relating x and y (Eq. 2.1),

$$y = x\left(1 + \frac{2C}{1 + |x|^2}\right).$$ (3.4)

From the steady state of Eq. 3.1, we see that $y = x - 2CP$. There are two contributions to y: x, and the collective polarization $2CP = -2Cx/(1 + |x|^2)$. For intermediate intensities ($x \sim 1$), the polarization is nonlinear. For low intensities ($x \ll 1$), however, the system is still linear, and Eq. 3.4 reduces to $y = x(1 + 2C)$.

To analyze the eigenvalues of the plane wave ring cavity configuration we linearize the set of five equations about their steady state values. For this analysis we assume that $\gamma_\parallel = 2\gamma_\perp$, *i.e.* there is only radiative broadening of

the atoms. The variables take the form

$$\eta = \bar{\eta} + \xi, \tag{3.5}$$

where

$$\eta = (x, x^*, P, P^*, D)^T, \tag{3.6}$$

$$\bar{\eta} = (x, x^*, -x/(1 + |x|^2), -x^*/(1 + |x|^2), -1/(1 + |x|^2))^T, \tag{3.7}$$

and

$$\xi = (\Delta x, \Delta x^*, \Delta P, \Delta P^*, \Delta D)^T \tag{3.8}$$

Here the T denotes transpose. ξ obeys the linear equations

$$\frac{d\xi}{dt} = \mathbf{A}\xi. \tag{3.9}$$

The eigenvalues of the system, are governed by $\mathbf{A}$:

$$\mathbf{A} = \begin{bmatrix} -\kappa & 0 & 2\kappa C & 0 & 0 \\ 0 & -\kappa & 0 & 2\kappa C & 0 \\ -\gamma_\perp/(1 + |x|^2) & 0 & -\gamma_\perp & 0 & \gamma_\perp x \\ 0 & -\gamma_\perp/(1 + |x|^2) & 0 & -\gamma_\perp & \gamma_\perp x^* \\ \gamma_\perp x^*/(1 + |x|^2) & \gamma_\perp x/(1 + |x|^2) & -\gamma_\perp x^* & -\gamma_\perp x & -2\gamma_\perp \end{bmatrix} \tag{3.10}$$

We find the eigenvalues of $\mathbf{A}$ numerically for different values of the intra-cavity field x. By then using Eq. 3.4, we have a relation between y and the eigenfrequency.

We modify the Maxwell Bloch equations in a manner following Lugiato [29, 30] in order to properly take the mode function of the cavity into account. The mode function $u(r)$ must be normalized such that $\int_V u^2(r)d^3r = 1$. The model in [29] which we follow incorporates only a Gaussian transverse profile, and has a normalization of unit length, with the following mode function:

$$u(r) = \sqrt{\frac{2}{\pi\omega_0}} e^{-\rho^2} \tag{3.11}$$

with a normalized x and y of

$$x_{\mathrm{G}} = \sqrt{\frac{2}{\pi\omega_0}} x_{\mathrm{pw}} , \quad y_{\mathrm{G}} = \sqrt{\frac{2}{\pi\omega_0}} y_{\mathrm{pw}}, \tag{3.12}$$

where ρ is the radial dimension in the cavity, in units of the cavity mode waist. We also have to include the standing wave, so the mode function is:

$$u(r) = \sqrt{\frac{4}{\pi\omega_0}} \cos(2\pi z) e^{-\rho^2}, \tag{3.13}$$

where z is the axial distance in the cavity. For purposes of comparison, we keep the normalizations of Eq. 3.12 and modify the Maxwell Bloch equations to obtain

$$\frac{dx(t)}{dt} = -\kappa \left[x(t) - y - 2C \int_0^1 \int_0^\infty d\rho\, dz\, 4\sqrt{2}\rho e^{-\rho^2} \cos(2\pi z) P(\rho, z, t) \right], \tag{3.14}$$

$$\frac{\partial P(\rho, z, t)}{\partial t} = \gamma_\perp [x(t) D(\rho, z, t) \sqrt{2} e^{-\rho^2} \cos(2\pi z) - P(\rho, z, t)], \tag{3.15}$$

$$\frac{\partial D(\rho, z, t)}{\partial t} = \tag{3.16}$$
$$-\gamma_\parallel \left\{ \frac{1}{2} [x(t) P^*(\rho, z, t) + x^*(t) P(\rho, z, t)] \sqrt{2} e^{-\rho^2} \cos(2\pi z) + D(\rho, z, t) + 1 \right\},$$

where again we have the complex conjugate equations of Eq. 3.14 and Eq. 3.15 governing x^* and P^*. By setting the time derivatives in Eqs. 3.14–3.16 to zero, one can calculate the steady state equation relating input and output intensities:

$$y = x + \frac{4C}{x} \ln(1/2 + 1/2\sqrt{1 + 2|x|^2}). \tag{3.17}$$

In the low intensity limit ($x \ll 1$), Eq. 3.17 reduces to $y = x(1 + 2C)$, as did Eq. 3.4. The form of Eq. 3.17 is slightly different than Eq. 2.1 with Eq. 2.2 because of our normalization for x and y. For direct comparison to [29] we used n_0 appropriate for that case, which differs by that in Eq. 2.1 by 3/4. Applying that scaling to Eq. 3.17 recovers the steady state equation for a Gaussian beam Fabry-Pérot cavity found in Chapter 2. The steady state equation is used to check our numerical simulations for accuracy, and to establish y_{crit}, the smallest y for which there is on-resonance bistability, for various values of C. Figure 3.1 shows a bistability curve generated with Eq. 3.17 for $C = 50$.

We numerically integrate Eqs. 3.14–3.16 by discretizing along the z axis from 0 to 1 and along the ρ axis from 0 to 3, each into 10 units. We then have a 10 by 10 grid which represents a radial section of the mode volume, which results in 302 differential equations: one each for x and x^*, 100 each for P and P^*, and 100 for D. We integrate the equations using an algorithm for solving stiff equations. We found the MATLAB routine ode23s to be suitable, if slow. The radial dimension is integrated up to $\rho = 3$. We have found this grid to be sufficiently fine to reproduce results found with a finer grid. We have also integrated ρ farther, and found no differences with our present results.
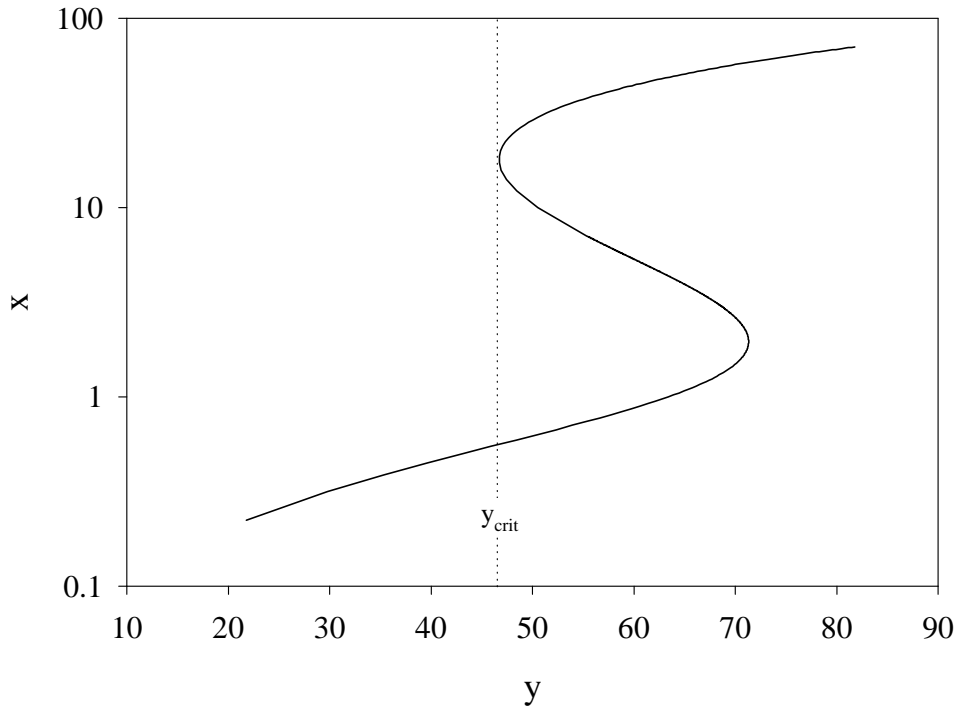
Figure 3.1: Intensity bistability curve generated with Eq. 3.17 for $C = 50$. y is proportional to the input field, and x is proportional to the field inside the atom-filled cavity. y_{crit} $(= 46.7$ in this case) is the lowest value of y for which there is on-resonance bistability.

This numerical integration gives the time response to an arbitrary step excitation taking into account the spatial variation of the mode function. To model the actual output for different input intensities, we start the numerical integration of Eqs. 3.14–3.16 with the system in the ground state and impose a driving term y starting at time $t = 0$. The driving field is a Heaviside step function multiplied by y. For a turn-off, the initial conditions for the 302 equations are taken from a turn-on simulation which has already reached steady state, and the driving term y is a complimentary Heaviside step function. An example is shown in Fig. 3.2. The upper plot shows the input drive term y. The lower plot shows the intracavity intensity $|x|^2$. From this result we can extract the eigenvalues of the system. We will use them later to compare with experimental results, and need to know them well.

Since the system we are studying is nonlinear, the eigenvalues change as a function of input intensity, so we must find their local value at a particular input intensity. From the time response we find the oscillation frequency. By repeating the calculation for different values of y we can find the change in the eigenvalues as a function of input intensity. In practice, we find a local eigenvalue in the following way. If we set the initial conditions very close to the steady state, the system will oscillate at its eigenfrequency Ω_{VR}. At very low input intensities, the eigenvalue is at Ω_0, the vacuum Rabi frequency predicted by Agarwal [2]. By doing repeated numerical integrations at increasing input fields, we find a curve representing the eigenvalue as a function of input intensity. After a numerical integration of the field x is complete, we subtract the steady state value and then use only the results after the first zero crossing
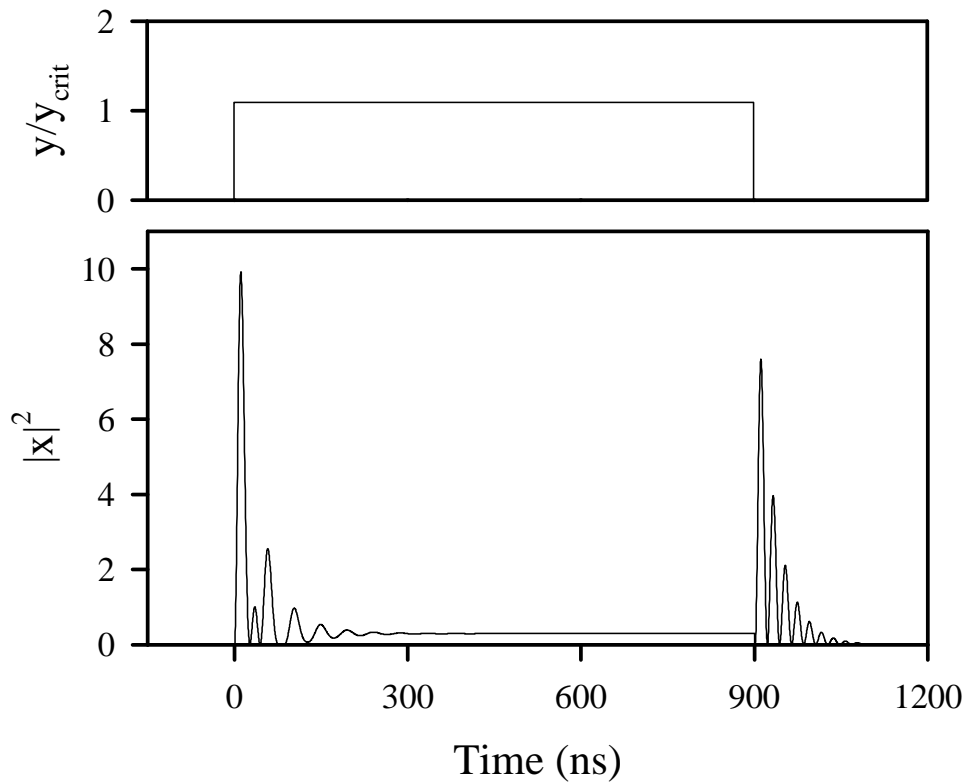
Figure 3.2: Numerical simulation incorporating the mode function of the cavity, using Eqs. 3.14–3.16. The upper plot shows the input driving term y, and the lower plot the intracavity intensity $|x|^2$.

following a maximum. The resulting function is then anti-symmetrized to produce a function whose integral is zero (eliminating a zero frequency component in the Fourier transform), and we take its Fourier transform. We fit the peak in the Fourier transform to a Lorentzian lineshape, and take its center to be the eigenfrequency. An example of the time response and the Fourier transform is shown in Fig. 3.3. The real part of Eq. 2.7 shows that the decay rate of the combined atom-cavity system should be $(\kappa + \gamma_\perp)/2$. For very low intensities ($x \ll 1$), we can use this as a guide to analyze the numerical simulation. We integrate Eqs. 3.14–3.16 for $y = 0.01 y_{\mathrm{crit}}$, which gives a steady state x of 0.005. The half width of 3.1 MHz is close to $(\kappa + \gamma_\perp)/2 = 3.05$ MHz, indicating that the numerical integration algorithm and the FFT procedure are doing a reasonably good job of extracting the longer time scale decay envelope of the oscillations as well as the shorter period oscillations themselves.

To stress the importance of the spatial dependence at higher input intensities, a comparison of the eigenfrequencies for the two sets of Maxwell Bloch equations is shown in Fig. 3.4, one for a plane travelling wave mode and the other for a Gaussian beam standing wave mode. The behavior is qualitatively different between the two sets. The solid lines are from the eigenvalues for the plane travelling wave case (Eq. 3.10). The dashed lines are for the Gaussian beam standing wave case, obtained from the procedure outlined above for different values of y. The abscissa is Y/Y_{crit}, where $Y \equiv y^2$. y_{crit} is the smallest value of y for which on-resonance bistability occurs, calculated separately for each C for the two sets with Eqs. 3.4 and 3.17. There is significantly more change with frequency for the standing wave Gaussian beam case than for the
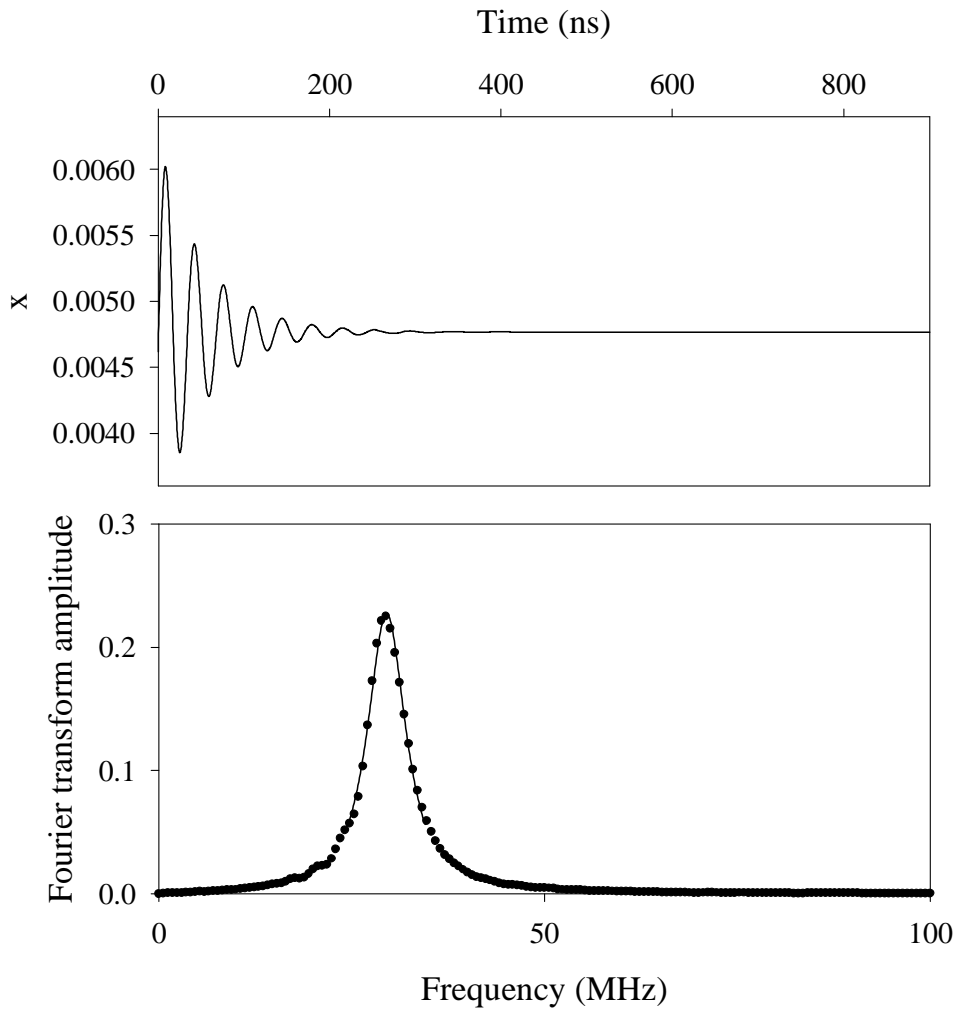
Figure 3.3: FFT of the output from Eqs. 3.14–3.16, for $y = 0.01y_{\mathrm{crit}}$, $C = 50$, $\kappa = \gamma_{\perp}$. The solid line is a fitted Lorentzian used to determine the center frequency.

plane wave ring cavity solution.

3.3 Experiment

In this experiment the apparatus is similar to that described in Chapter 2. The heart of the apparatus [28] is a high finesse optical cavity formed by two 1.3 cm diameter mirrors, each with radius of curvature of 7.5 cm and transmission coefficient of 2.4×10^{-4}, separated by 4.1 mm (see Fig. 3.5). An oven heated to ≈ 430 K produces an effusive beam of Rb atoms that are optically pumped before intersecting the cavity mode at $90°$. This provides a continuous stream of two-level atoms that on the average spend 11 lifetimes crossing the waist of the TEM_{00} Gaussian mode of the cavity. The parameters of the experiment are $(g, \kappa, \gamma_\perp) = 2\pi(1.5, 1.38 \pm 0.02, 3.04) \times 10^6$ rad/sec, falling in the intermediate regime of cavity QED. The excitation source is a cw Ti:Sapphire laser locked on resonance to the $5S_{1/2}, F = 3 \rightarrow 5P_{3/2}, F = 4$ transition of ^{85}Rb. Part of the laser beam is split into an intense auxiliary beam to lock the cavity on resonance using FM sidebands [31]. The other beam, much weaker in intensity, serves as the signal beam. A chopper wheel alternatively passes the locking or the signal beam at a rate of ≈ 1 kHz. The signal and lock beams are mode-matched into the cavity. The beam emerging from the cavity passes through a beam splitter by which 8% of the beam is split off and sent to a PMT to monitor the lock beam. The remainder of the beam is sent to a photon counting detector, discussed below.

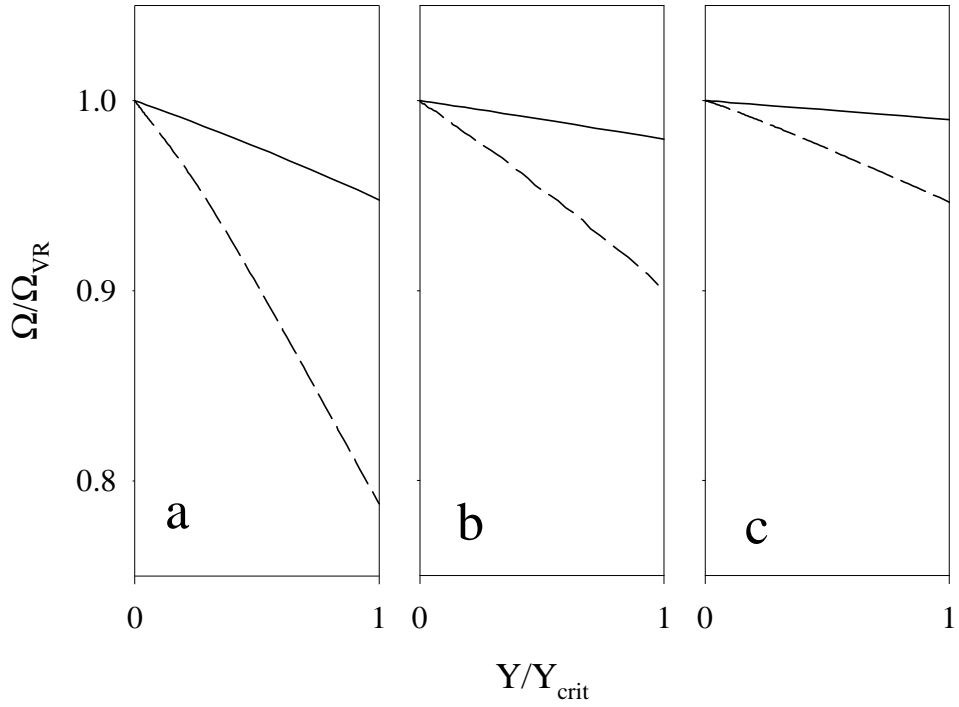While the locking beam is blocked, the signal beam is turned on and off

Figure 3.4: Eigenfrequencies for the plane wave and Gaussian beam transverse mode function sets of Maxwell Bloch equations as a function of input intensity. The solid lines are from the plane wave model, and the dashed lines from the Gaussian beam standing wave model. $\kappa = \gamma_\perp = \gamma_\parallel/2$. For plots a, b, and c, $C = 20$, 50, and 100, respectively.

with a 4 μs period by two electro-optic modulators (EOM) in series (Gsänger LM0202 with Gsänger LIV 8 controllers). A Stanford DS345 synthesized function generator provides start pulses for the time-to-digital converter, and a trigger pulse for a Stanford DG535 digital delay/pulse generator, which itself produces TTL pulses for the EOM controllers. A signal from the chopper wheel gates the triggers from the DS345, so that the probe light is off while the lock beam passes, and chopping when the probe beam passes.

We used an on:off period ratio of 1:3 rather than 1:1, which enhanced the performance of the EOMs. The turn-off response of the signal beam intensity after the EOMs closely fits a Gaussian curve with a half-width of 9 ns, and has been carefully studied for use in another experiment.[32] The turn-off 90%–10% time is 12.5 ns. The turn-on has a similar response, but is slightly faster, with a 10%–90% time of 9 ns. The extinction ratio between the turn-off time t_0 and time $t_0 + 20$ ns is 250:1. The output decays roughly exponentially for the next 250 ns, reaching an on:off ratio of 400:1 at $t_0 + 25$ ns and 1200:1 at $t_0 + 270$ ns. The intensity decreases linearly for the next 2.5 μs by a factor of two. The alignment of the EOMs is delicate. An initial adjustment may be made while in dc mode, while the EOMs stay in their "off" position. The on:off ratio of each one in dc mode can be 300:1, but when switched with a 4 μs period, the ratio for the two in series is only ∼200:1. Further adjustment while switching is necessary to reach the extinction ratios quoted above. For use in another experiment [32], where the extinction is more critical, ratios of 800:1 have been reached for $t_0 + 25$ ns. All of the above numbers are from histograms compiled from many turn-offs, and are not sensitive to different

contributions from a finite time turn-off and jitter in the exact turn-off time relative to the pulse which triggers the histogram.

The EOMs and their controllers are located 2.5 m from the photon counting detector, which poses some problems. The controllers emit a large amount of rf radiation as they switch the high voltage on and off. We initially used a PMT (Hamamatsu R636-10) in photon counting mode as our detector, with no preamplifier, so the photoelectric pulses had to travel several meters to the counting electronics. The pulses were discriminated by a Stanford SR400 gated photon counter, but the rf from the EOM controllers caused false counts near the turn-on and turn-off times. Shielding of cables and the installation of an rf cage around the controllers did not bring the stray pulses under control. Oscillations in the count rate of 30% were typical, with a period of ≈ 18 ns. The rf problems were not too bad with a single EOM, but with two EOMs the problems were such that the PMT was not a useful tool.

We switched detectors to an EG&G SPCM-AQ-151, an avalanche photo-diode (APD) packaged on a Peltier cooler, with discrimination circuitry. The package is powered by a 5 V supply, and returns TTL pulses when it detects a photon. The quoted detection efficiency of this model is 50% at 780 nm. We measured a dark count rate of 27 counts per second and a dead time of 28 ns. The EG&G module is significantly more immune to the rf from the EOM controllers. The TTL pulses pass through a discriminator and are converted to NIM by the SR400 (which has a bandwidth of 200 MHz), then converted again to ECL (with a LeCroy 4616). A LeCroy 3377 time to digital converter (TDC) starts with a gated pulse originating from the DS345 converted to NIM

(with a LeCroy 688AL) then to ECL, and registers a hit for each signal from the APD, up to 16 hits per start during the 4 μs data collection. The TDC has 0.5 ns time resolution, with 10% differential nonlinearity. The differential nonlinearity indicates the percentage difference that a given bin width may be from 0.5 ns. We have calibrated the overall time scale with a known delay to 0.25%. The times are dumped to a LeCroy 4302 memory unit, and then read into a computer via an IEEE-488 bus and compiled into a histogram (see description in the appendix).

3.4   Results

During a data run, we let the oven temperature stabilize and then perform a measurement of the on-resonance intensity bistability, by sweeping the signal beam intensity and recording the output characteristics (see Fig. 2.2) [28]. This scan identifies I_{crit}, the lowest input intensity at which there is on-resonance bistability [26]. We then fix the signal beam input intensity and collect data which we store in a histogram. This is repeated for different values of the input intensity, both above and below I_{crit}. We also explore other coupling strengths $(g\sqrt{\bar{N}})$ by changing the number of atoms with the oven temperature (the smallest value was $\bar{N} = 25$). The results are qualitatively similar to those presented here.

Fig. 3.6a shows the response of the system to a step excitation of $1.2I_{\mathrm{crit}}$ for an effective number of atoms in the cavity mode of $\bar{N} \approx 300$. The input intensity is lower than the turn-up point in optical bistability (see Fig. 2.2), so

the steady state of the system is always on the lower branch. The transmitted intensity grows from zero and then turns over once the atoms start building up a polarization that then exchanges energy with the cavity mode. The measured intensity oscillates at two frequencies, because the output field is composed of a part oscillating at approximately Ω_{VR} and the slow build up of a steady state field ($x < 1$). For the first part of the turn-on, the oscillations in the field are around zero and large enough that they cause an intensity oscillation at $2\Omega_{VR}$. At the end, field and intensity both oscillate at Ω_{VR} since the amplitude of the oscillations are smaller than the steady state. Fig. 3.6b shows the freely evolving system after the sudden turn-off of the excitation. The frequency of oscillation in this case is twice the frequency of oscillation of the field. Note that the intensity first decreases and then grows to a value much larger than the steady state. There is a large amount of energy stored in the atomic polarization opposing the incoming field. This can easily be seen in the low-intensity-limit form of the state equations, Eq. 3.4 or Eq. 3.17, $y = x(1 + 2C)$, as noted before (Section 3.2). Recall that y is the intracavity field in the absence of atoms, while x is the intracavity field in the presence of atoms. The contribution of the collective polarization is $2C$ times that which is free in the cavity. When the incoming field is turned off, the steady state equilibrium is disturbed, and the energy is free to go into the cavity. From there it can escape, but part of it returns to the atoms. We can observe more than 12 exchanges before the signal decays into the background noise (see inset on Fig. 3.6b).

Fig. 3.7 shows theoretical results for the same parameters as in Fig. 3.6,

with the turn-on and turn-off as Heaviside step functions. The relative scaling of the frames in each set of figures is the same to allow for comparison. The height of the oscillations relative to the steady state is much greater in the theoretical plots than in the data. For the turn-on, the ratio is 34 for the theory, and 9.4 for the data. The turn-off ratios are 26 for the theory, and 5.8 for the data. The frequencies of oscillation, however, agree very well.

A calculation with the same parameters as in Fig. 3.7, but with a nonzero background, is shown in Fig. 3.8. The steady state level before the turn-on is $x = 0.13$, so $|x|^2 = 0.018$. This corresponds to an input intensity of I/I_{crit} of 0.1. The turn-off is from the higher steady state level back to $x = 0.13$. The size of the oscillations with respect to the background changes dramatically with respect to Fig. 3.7. The ratio of peak to steady state for the turn-on is 19, and for the turn-off is 11.

One notable feature of the experimental data in Fig. 3.6 is that the oscillations do not go to zero, even though the frequency is $2\Omega_{\mathrm{VR}}$, indicating that the field oscillations are large enough to go through zero. In Fig. 3.8 the oscillations in the turn-off go to zero even in the presence of a large background from an input intensity of $I/I_{\mathrm{crit}} = 0.1$. The residual background from an incomplete turn-off is much smaller. In Fig. 3.6b, the dip between the first and second big peaks has a lowest level of $\approx 1/4$ the steady state value, while the input intensity is down to 1/400 its steady state at that time, $I/I_{\mathrm{crit}} = 1.2/400$. The troughs still do not go to zero at $t_0 + 200$ns, but do oscillate at $2\Omega_{\mathrm{VR}}$, unlike Fig. 3.8. A finite time turn-off is well over by that point. In addition, no rf noise was detected in the turn-off region with the APDs.

One possible cause lies in the jitter between the turn-off time and the start trigger time for the histogram. As was noted above, our means of characterizing the turn-off pulses cannot distinguish between jitter and a finite turn-off time, but the ringing response would be quite sensitive to jitter. Using the theoretical plot from Fig. 3.7, and summing over a Gaussian distribution of starting times with $\sigma = 2$ns, we get a time response with raised troughs similar to the data. A comparison of such a simulation and the data is shown in Fig. 3.9. For ease of comparison, the theory has an added background of 0.01. The beginning of the signal does not agree between the two because the size of the oscillations in the theory is much larger (with regards to the steady state) than the experimental results. Hence the initial dip in the theory is much more sensitive to jitter. The agreement with this simulation is quite good, suggesting that part of the observed turn-off time is caused by a variation in the turn-off time with respect to the histogram. It is important to note that this type of variation will only affect the amplitude of the signals, not their frequency. The jitter is equivalent to adding together sets of oscillations which are out of phase:

$$\cos(\omega t + \phi_1) + \cos(\omega t + \phi_2) = r\cos(\omega t - \Phi) \qquad (3.18)$$

where $r = 2\cos[(\phi_1 + \phi_2)/2]$ and $\cos\Phi = (\cos\phi_1 + \cos\phi_2)/r$, which does not change the frequency of oscillation.

Using the plane wave model as a guide, the theoretical decay rate of the field of the atoms-cavity system is $(\kappa + \gamma_\perp)/2$, which in this case is $2.22 \pm 0.05 \times 2\pi \times 10^6$ rad/s, neglecting any broadening of $\gamma_\perp$. To find the decay constant

from the turn-off response, we take the fast Fourier transform of the turn-off, starting at the peak of the first oscillation, extending for 2.5 μs. The Welch window [33] is applied to the data before taking the Fourier transform. This window multiplies the data by a function which drops to zero at the edges, and reduces the size of sidelobes next to the peaks. A set of Lorentzians is then fit to the FFT amplitude. The Fourier transform of $e^{-\beta x} \cos^2(\alpha x)$ is a set of Lorentzians, one centered at zero, and one at the oscillation frequency. This procedure on simulated data with a decay constant of 30×10^6 rad/s yields the correct width with a 1% accuracy.

The Fourier transform of the time response with accompanying Lorentzian fit is shown in Fig. 3.10. The fit is of three Lorentzians, one of which is forced to be centered at zero, and is performed with the MATLAB routine fmins, which uses a Nelder-Mead type simplex search method. The large peak is at $2\Omega_{VR}$, since we measure the intensity of the output light, and exchange of energy between the atoms and the field is taking place at Ω_{VR}. A small amount of the fundamental frequency is also visible in the figure. The best fit for the fundamental frequency is half of that of the big peak to within 1%. The width of both the Lorentzian centered at zero and the one at $2\Omega_{VR}$ have a FWHM of 9.8 ± 0.2 MHz, with the uncertainty estimated by the agreement between the two, and by the inherent accuracy of the procedure. The decay constant of the field then is $2.45 \pm 0.10 \times 2\pi \times 10^6$ rad/s. The difference between this number and the 2.22 quoted above gives us an idea of the size of broadening mechanisms affecting the atoms. For comparison, Fig. 3.11 shows the turn-off response of the cavity without atoms present. The curve is exponential, and

gives the decay constant of the cavity. Fitting a line to the data in Fig. 3.11 gives a decay constant of $1.38 \pm 0.02 \times 2\pi \times 10^6$ rad/s, in agreement with and much more precise than our measurement of 1.4 ± 0.1 MHz for the half width half maximum of the cavity resonance, made by scanning the cavity length with a piezo-electric transducer across resonance with the laser frequency fixed.

3.5   Conclusions

Fig. 3.12 shows the frequency of oscillation of the output field as a function of the input intensity, obtained from the fast Fourier transform of the time response. The dashed and dotted lines come from the time-response calculations, when the driving field is suddenly turned on and off. As Fig. 3.4 shows, these curves are much different than the corresponding behavior in a plane wave ring cavity. The turn-on has a frequency shift towards smaller values for larger input intensities. The system is driven and oscillates in the non-linear regime. The uncertainties are limited by the ability of the Fourier transform to extract the correct frequency. Fig. 3.13 is a comparison of the frequencies obtained from the time response measurements and from the spectroscopic measurements described in Chapter 2. The solid line is the prediction for the evolution of the anharmonic vacuum Rabi peaks as the intensity of the spectroscopic probe changes, using parameters appropriate for the experimental data. It describes the condition that there be no phase shift between input and output fields (see Section 2.2). Although the experimental conditions for the time and frequency observations are different, the scaling of frequencies

and intensities with Ω_0 and I_{crit} permits a direct comparison. The model predictions for the two different Ω_0, and I_{crit} realized in the experiments differ at most by 8% at the highest intensity. The oscillation frequency of the turn-off response is fairly constant at Ω_0 since the system oscillates at low intensity (no drive) most of the time. The data obtained spectroscopically follow closely the zero-phase condition, eventually merging the two peaks into a single one for $I \approx I_{\mathrm{crit}}$. The values obtained in the small intensity region $I/I_{\mathrm{crit}} \ll 1$ show two distinct features. First, the spectroscopy and the time domain measurements reach the same value of the oscillating frequency $\Omega_{\mathrm{VR}}/\Omega_0$. In this regime, the system is linear and its response to step excitation gives the same information as the transmission spectroscopy. Second, the slopes of the curves are very different at $I/I_{\mathrm{crit}} = 0$. The zero phase condition Eq. 2.9, established in the driven system between the input and output fields, creates a relationship between the oscillating frequency Ω_{VR} and the intensity I. Its derivative with respect to the intensity is non-zero even for zero intensity as shown by the theoretical curve.

The spectrum obtained for the coupled atoms-cavity system by analyzing the time response to step excitation shows the oscillatory exchange of energy with an excitation dependent period. Despite a high excitation for the turn-off time response, the system oscillates at the low intensity frequency, providing no information of the possible non-linear regime. The turn-on time response frequency shows an intensity dependence, demonstrating that the resulting behavior is a probe of the eigenvalues of the system at a finite input intensity. The frequency dependence is much different than in the spectroscopic case de-

scribed in Chapter 2. From the agreement between the theory and experiment in the frequencies of oscillation, however, it is evident that a frequency measurement in the system may be a more reliable means to extract quantitative information than the absolute heights of signals.

The turn-off measurements also give good agreement with theory in their decay rates, both with atoms and without. With no atoms present, it is possible to extract very precisely the decay constant of the cavity. When measuring a decay rate of the atoms-cavity system, the peaks give both the average decay rate of the system and the frequency of oscillation.

In more general terms, we have made a conditional measurement of the dynamics of the atoms-cavity system. The condition in this case is the sudden turn-on or turn-off of the input light from steady state. The excitation or de-excitation comes from the field, not from the atoms. This is contrary to experiments in the microwave regime such as those in the group of Haroche [6], in which the atoms enter the cavity in an excited state. A conditional intensity measurement can be a very powerful tool, and we learned several things about its use in this case.

In order to probe the nonlinearities of the system, we need to use a conditional measurement which leaves the system (finally) in a non-zero steady state. For the turn-off measurements, the absence of a driving field left the system free to evolve towards a steady state with no energy in it. The results show only the basic harmonic structure of two coupled oscillators, one corresponding to the polarization and the other to the field. On the other hand, the turn-on measurements allowed us to probe the response of the system as it

was coming to a steady state with non-zero energy, which provided information about the eigenfrequencies of the system at that steady state.
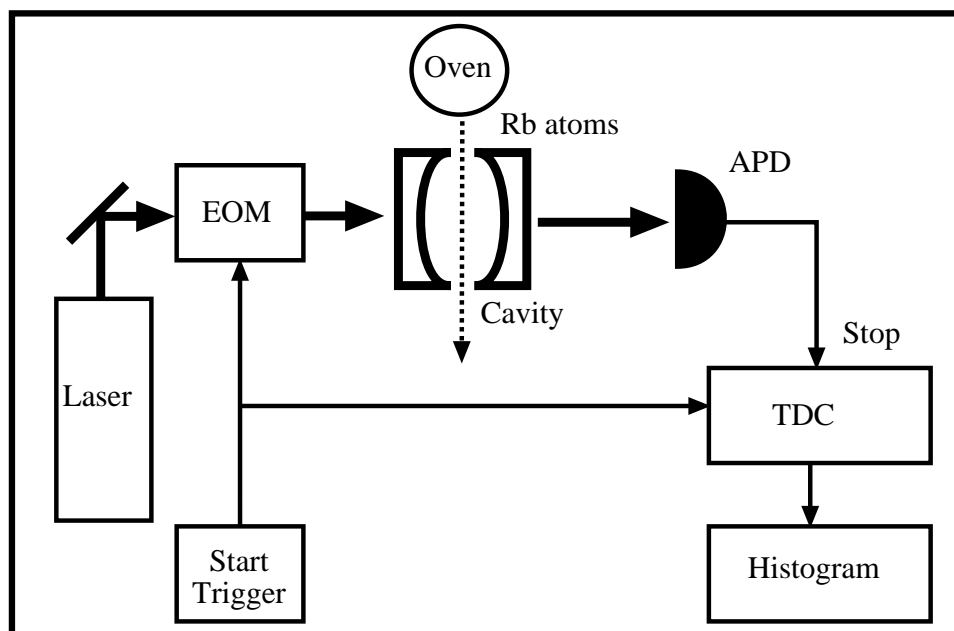
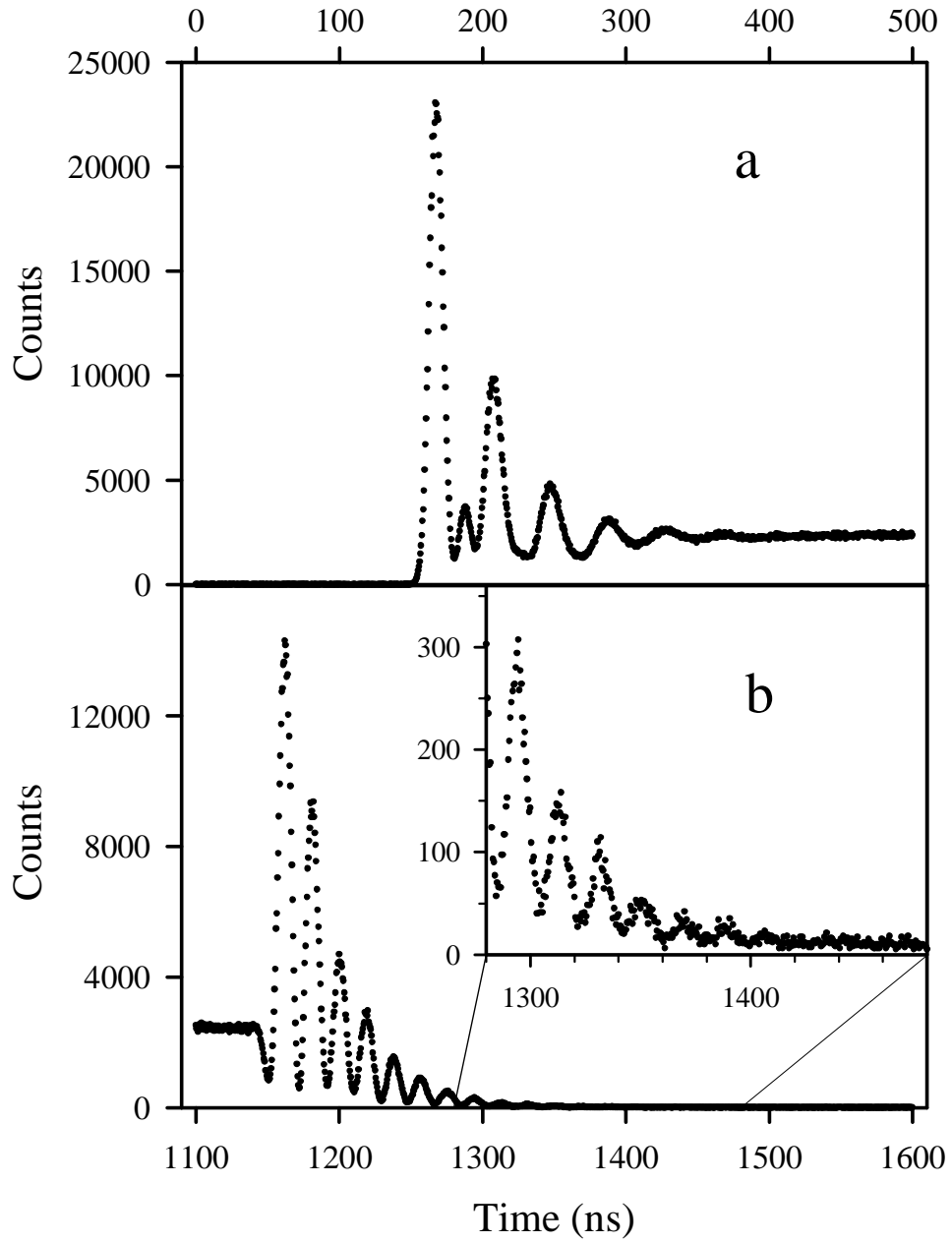Figure 3.5: Simplified diagram of the experimental setup.

Figure 3.6: Time response of the coupled atoms-cavity system to turn-on (a) and turn off (b) step excitation of $I/I_{\mathrm{crit}} = 1.2$. The inset is an amplification by a factor of 30 of the vertical scale.
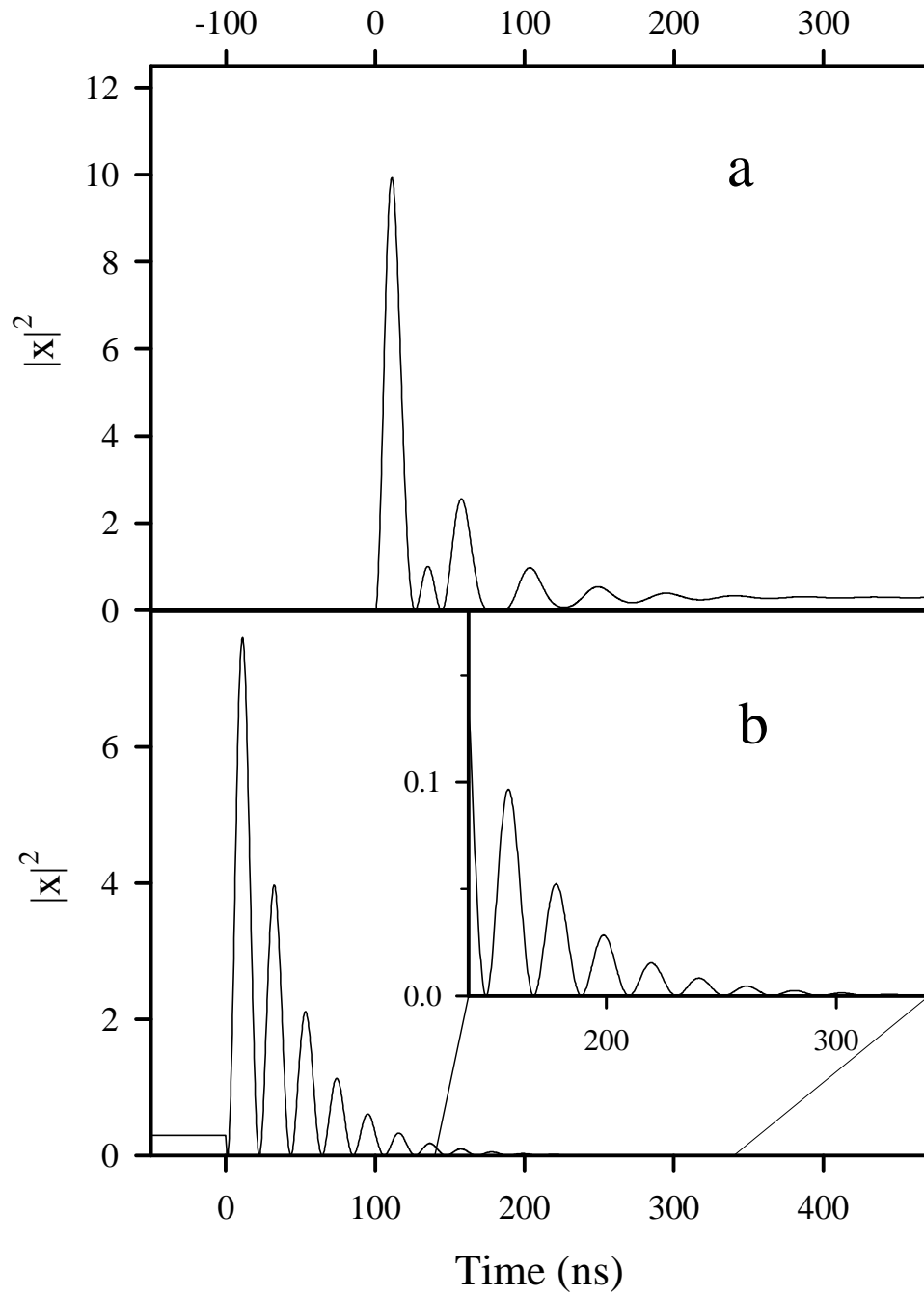
Figure 3.7: Theoretical curves from a numerical integration of Eqs 3.14–3.16 for the same parameters as in Fig. 3.6.
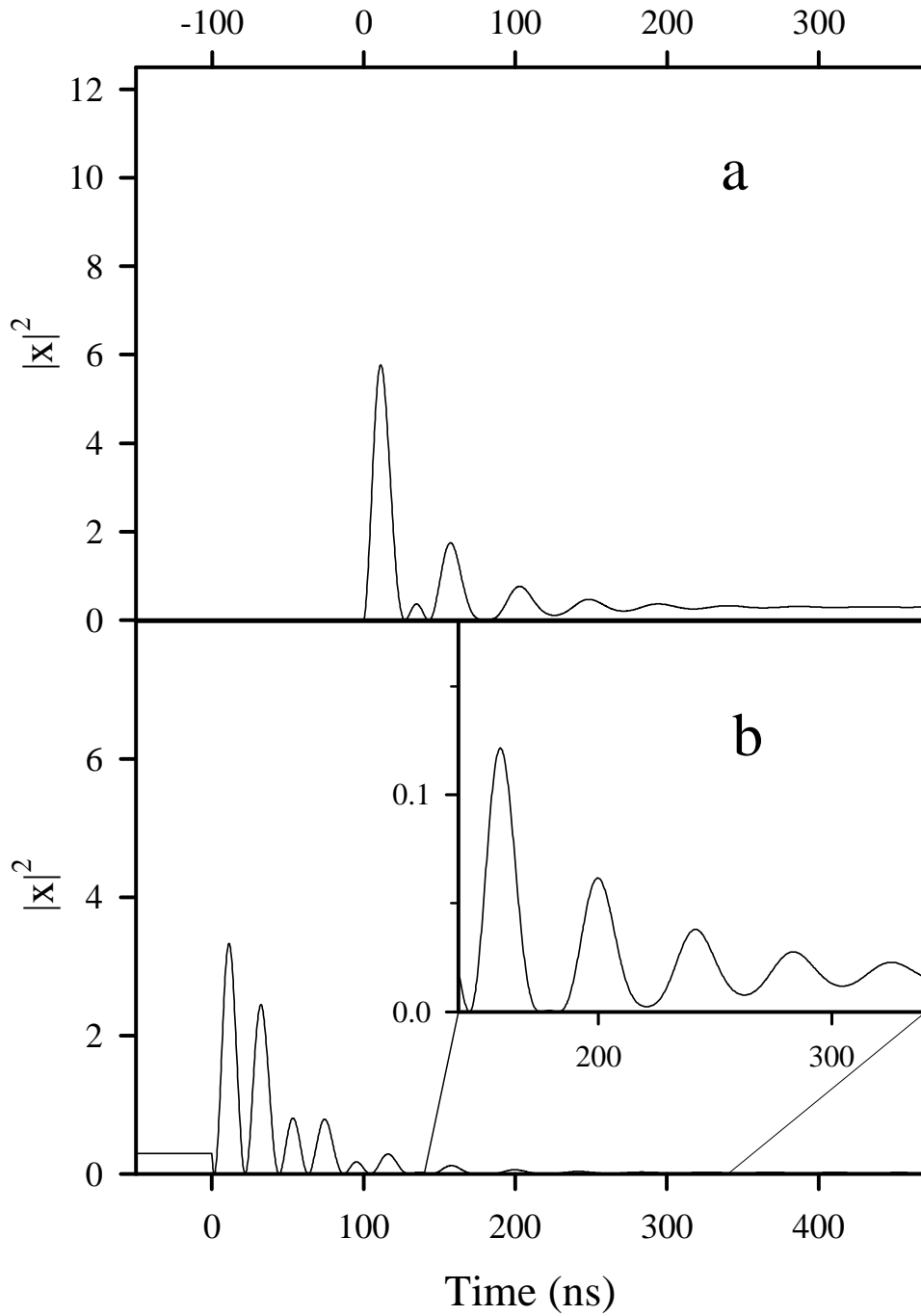
Figure 3.8: Theoretical curves from a numerical integration of Eqs 3.14–3.16 for the same parameters as in Fig. 3.6, with a steady state background of $|x|^2 = 0.018$.
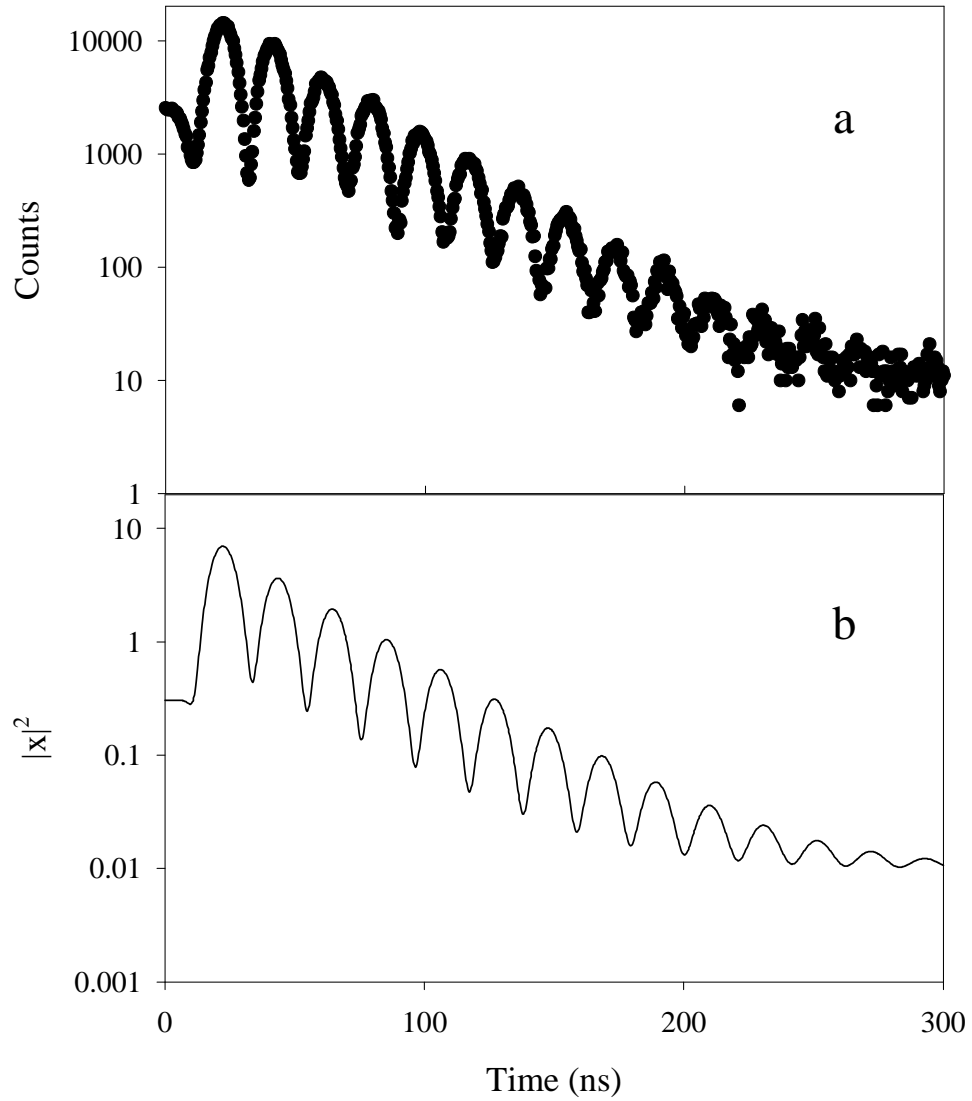
Figure 3.9: Data from Fig. 3.6b compared to a theoretical curve from Fig. 3.7 with a Gaussian distribution of starting times with $\sigma = 2$ ns. The theory has an imposed background of 0.01.
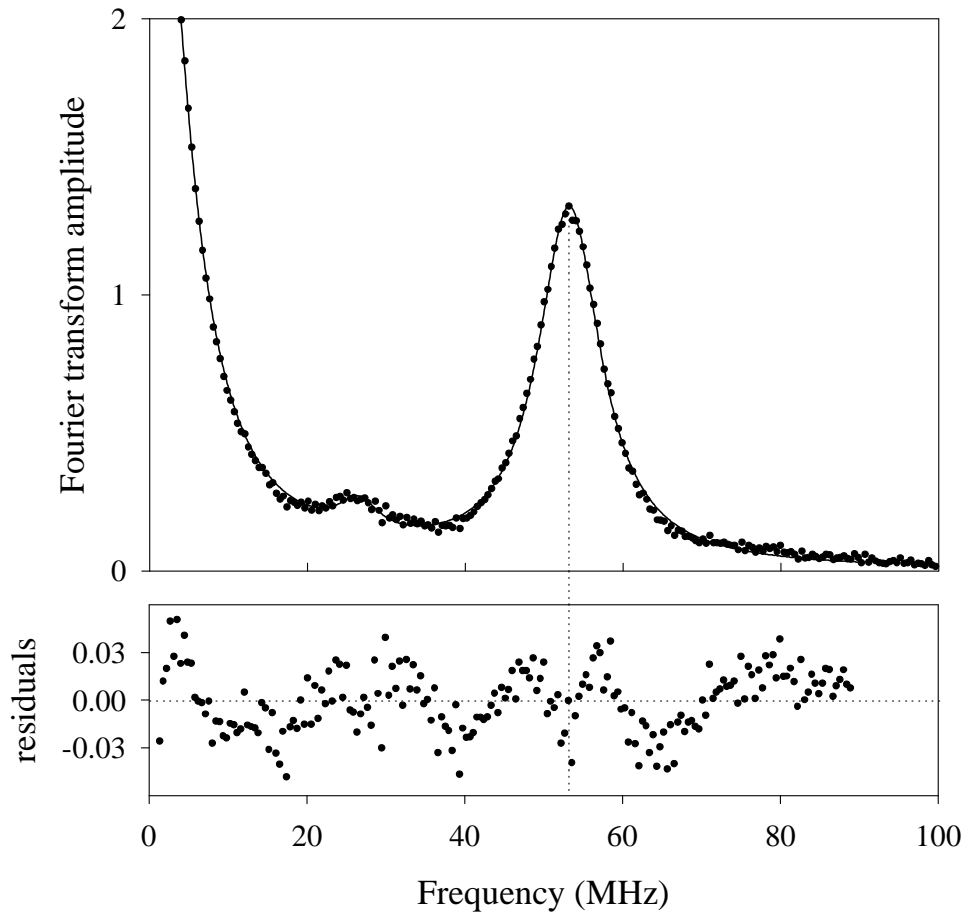
Figure 3.10: FFT of the turn-off in Fig. 3.6. The curve is a fit of three Lorentzians. The large peak is the second harmonic, which is dominant since the field is oscillating about zero. A small amount of the fundamental frequency is visible.
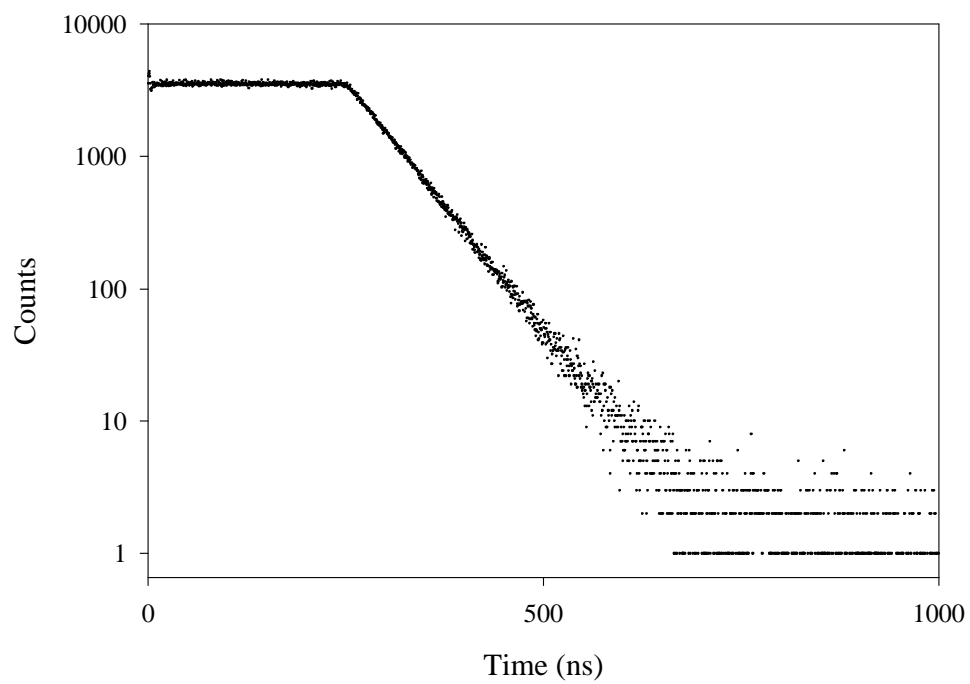
Figure 3.11: Turn-off response of an empty cavity. A line fit to the data gives a decay rate of $1.38 \pm 0.02 \times 2\pi \times 10^6$ rad/s.
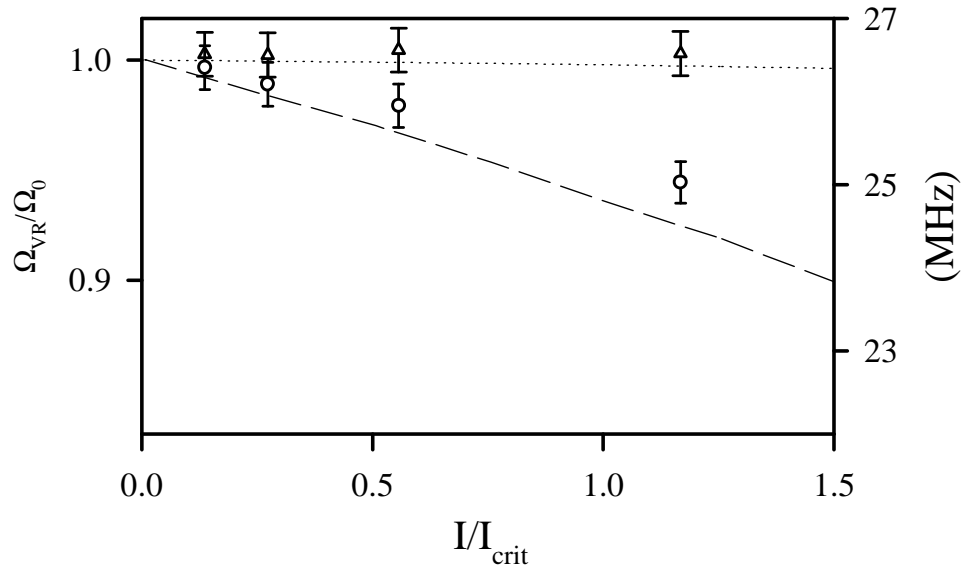
Figure 3.12: Frequency of the exchange of excitation as a function of input intensity measured by fast Fourier transform of the time response from turn-on (dashed line), and turn-off (dotted line). The empty circles (turn-on) and triangles (turn-off) come from data similar to Fig. 3.6 but for different driving intensities I/I_{crit}.
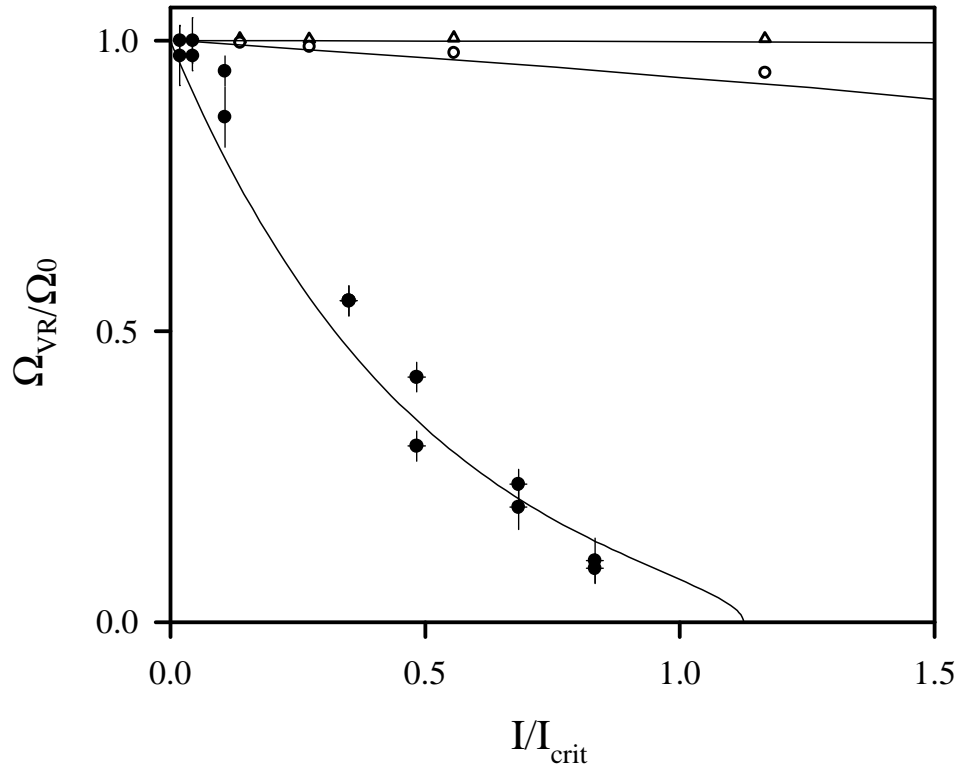
Figure 3.13: Comparison of data in Fig. 3.12 with the results from Chapter 2. The upper lines are from Fig. 3.12, while the lower curve and points are from the peak locations from transmission spectroscopy of the vacuum Rabi sidebands, Fig. 2.5.

Bibliography

[1] E. T. Jaynes and F. W. Cummings, Proc. IEEE **51**, 89 (1963).

[2] G. S. Agarwal, Phys. Rev. Lett. **53**, 1732 (1984).

[3] F. Bernardot, P. Nussenzveig, M. Brune, J. M. Raimond, and S. Haroche, Europhys. Lett. **17**, 33 (1992).

[4] M. G. Raizen, R. J. Thompson, R. J. Brecha, H. J. Kimble, and H. J. Carmichael, Phys. Rev. Lett. **63**, 240 (1989).

[5] C. Weisbuch, M. Nishioka, A. Ishikawa, and Y. Arakawa, Phys. Rev. Lett. **69**, 3314 (1992).

[6] Y. Kaluzny, P. Goy, M. Gross, J. M. Raimond, and S. Haroche, Phys. Rev. Lett. **51**, 1175 (1983).

[7] R. J. Brecha, L. A. Orozco, M. G. Raizen, M. Xiao, and H. J. Kimble, J. Opt. Soc. Am. B **12**, 2329 (1995).

[8] H. Wang, J. Shah, T. C. Damen, L. N. Pfeiffer, and J. E. Cunningham, Phys. Stat. Sol. (b) **188**, 38 (1995).

[9] M. Tavis and F. W. Cummings, Phys. Rev. **170**, 379 (1968).

[10] M. Tavis and F. W. Cummings, Phys. Rev. **188**, 692 (1969).

[11] J. J. Sánchez Mondragón, N. B. Narozhny, and J. H. Eberly, Phys. Rev. Lett. **51**, 550 (1983).

[12] R. J. Thompson, G. Rempe, and H. J. Kimble, Phys. Rev. Lett. **68**, 1132 (1992).

[13] J. Gripp, S. L. Mielke, L. A. Orozco, and H. J. Carmichael, Phys. Rev. A **54**, R3746 (1996).

[14] L. A. Lugiato, in *Progress in Optics*, edited by E. Wolf (North-Holland, Amsterdam, 1984), Vol. XXI, pp. 69–216.

[15] A. T. Rosenberger, L. A. Orozco, H. J. Kimble, and P. D. Drummond, Phys. Rev. A **43**, 6284 (1991).

[16] *Cavity Quantum Electrodynamics*, *Advances in Atomic, Molecular, and Optical Physics*, edited by P. R. Berman (Academic Press, Boston, 1994), supplement 2.

[17] M. G. Raizen, L. A. Orozco, M. Xiao, T. L. Boyd, and H. J. Kimble, Phys. Rev. Lett. **59**, 198 (1987).

[18] L. A. Orozco, M. G. Raizen, M. Xiao, R. J. Brecha, and H. J. Kimble, J. Opt. Soc. Am. B **4**, 1490 (1987).

[19] G. Rempe, F. Schmidt-Kaler, and H. Walther, Phys. Rev. Lett. **64**, 2783 (1990).

[20] G. Rempe, R. J. Thompson, R. J. Brecha, W. D. Lee, and H. J. Kimble, Phys. Rev. Lett. **67**, 1727 (1991).

[21] H. J. Carmichael, personal communication.

[22] M. Brune, F. Schmidt-Kaler, A. Maali, J. Dreyer, E. Hagley, J. M. Raimond, and S. Haroche, Phys. Rev. Lett. **76**, 1800 (1996).

[23] Y. Zhu, D. J. Gauthier, S. E. Morin, Q. Wu, H. J. Carmichael, and T. W. Mossberg, Phys. Rev. Lett. **64**, 2499 (1990).

[24] J. J. Childs, K. An, M. S. Otteson, R. R. Desari, and M. S. Feld, Phys. Rev. Lett. **77**, 2901 (1996).

[25] P. D. Drummond, IEEE J. Quant. Electron. **QE 17**, 301 (1981).

[26] J. Gripp and L. A. Orozco, Quantum Semiclass. Opt. **8**, 823 (1996).

[27] J. Gripp, Ph.D. thesis, State University of New York at Stony Brook, 1997.

[28] J. Gripp, S. L. Mielke, and L. A. Orozco, Phys. Rev. A **51**, 4974 (1995).

[29] L. A. Orozco, H. J. Kimble, A. T. Rosenberger, L. A. Lugiato, A. L. Asquini, M. Brambilla, and L. M. Narducci, Phys. Rev. A **39**, 1235 (1989).

[30] L. A. Lugiato and M. Milani, Opt. Comm. **46**, 57 (1983).

[31] R. W. P. Drever, J. L. Hall, F. V. Kowalski, J. Hough, G. M. Ford, A. J. Munley, and H. Ward, Appl. Phys. B **31**, 97 (1983).

[32] W. Z. Zhao, J. E. Simsarian, L. A. Orozco, W. Shi, and G. D. Sprouse, Phys. Rev. Lett. **78**, 4169 (1997).

[33] P. D. Welch, in *Modern Spectral Analysis*, *IEEE Press Selected Reprint Series*, edited by D. G. Childers (IEEE Press, New York, 1978), p. 17.

[34] H. J. Kimble, in *Cavity Quantum Electrodynamics*, *Advances in Atomic, Molecular, and Optical Physics*, edited by P. R. Berman (Academic Press, Boston, 1994), pp. 203–266, supplement 2. See Ref. [16].

[35] R. J. Brecha, Ph.D. thesis, University of Texas at Austin, 1990.

[36] R. J. Thompson, Ph.D. thesis, University of Texas at Austin, 1994.

[37] D. M. Meekhof, C. Monroe, B. E. King, W. M. Itano, and D. J. Wineland, Phys. Rev. Lett. **76**, 1796 (1996).

[38] R. Loudon, *The Quantum Theory of Light*, 2nd ed. (Oxford University Press, New York, 1983).

[39] L. Mandel and E. Wolf, *Optical Coherence and Quantum Optics* (Cambridge University Press, New York, 1995).

[40] P. R. Rice and H. J. Carmichael, IEEE J. Quant. Elect. **QE 24**, 1351 (1988).

[41] H. J. Kimble, M. Dagenais, and L. Mandel, Phys. Rev. Lett. **39**, 691 (1977).

[42] P. L. Knight and L. Allen, *Concepts of Quantum Optics* (Pergamon, Oxford, 1983).

[43] H. J. Kimble and L. Mandel, Phys. Rev. A **13**, 2123 (1976).

[44] H. J. Carmichael, S. Singh, R. Vyas, and P. R. Rice, Phys. Rev. A **39**, 1200 (1989).

[45] H. J. Carmichael, R. J. Brecha, and P. R. Rice, Opt. Commun. **82**, 73 (1991).

[46] H. J. Carmichael, Phys. Rev. A **33**, 3262 (1986).

[47] C. W. Gardiner, *Handbook of Stochastic Methods for Physics, Chemistry, and the Natural Sciences*, *Springer Series in Synergetics*, 2nd ed. (Springer-Verlag, Berlin, 1985).

[48] M. Xiao, H. J. Kimble, and H. J. Carmichael, Phys. Rev. A **35**, 3832 (1987).

[49] J. L. Hall, L. Hollberg, T. Baer, and H. G. Robinson, Appl. Phys. Lett. **39**, 680 (1981).

[50] J. Gripp, S. L. Mielke, and L. A. Orozco, Phys. Rev. A **56**, 3262 (1997).

[51] A. L. Lacaita, F. Zappa, S. Bigliardi, and M. Manfredi, IEEE Trans. Electron Devices **ED 40**, 577 (1993).

[52] G. T. Foster, S. L. Mielke, and L. A. Orozco, in *IQEC 1998* (Optical Society of America, Washington, DC, 1998).

[53] R. Short and L. Mandel, Phys. Rev. Lett. **51**, 384 (1983).

[54] H. Mabuchi, Q. A. Turchette, M. S. Chapman, and H. J. Kimble, Opt. Lett. **21**, 1393 (1996).

[55] G. M. Meyer, H.-J. Briegel, and H. Walther, Europhys. Lett. **37**, 317 (1997).

[56] K. Gibble and S. Chu, Phys. Rev. Lett. **70**, 1771 (1993).